Supporting Information

General Oriented Synthesis of Precise Carbon-Confined Nanostructures by Low-Pressure Vapor Superassembly and Controlled Pyrolysis

Jiashen Meng,[†,#] Xiong Liu,[†,#] Jiantao Li,[†] Qi Li,[†] Chuan Zhao,[‡] Linhan Xu,[§] Xuanpeng Wang,[†] Fang Liu,[†] Wei Yang,[†] Xiaoming Xu,[†] Ziang Liu,[†] Chaojiang Niu,[†,*] Liqiang Mai [†,ǁ,*]

[†]State Key Laboratory of Advanced Technology for Materials Synthesis and Processing, Wuhan University of Technology, Wuhan 430070, China.

[‡]School of Chemistry, Faculty of Science, The University of New South Wales, Sydney, New South Wales 2052, Australia.

[§]Department of Physics and Collaborative Innovation Center for Optoelectronic Semiconductors and Efficient Devices, Xiamen University, Xiamen 361005, China.

[ǁ]Department of Chemistry, University of California, Berkeley, California 94720, United States

[#]These authors contributed equally to this work.

[*]E-mail: mlq518@whut.edu.cn; niuchaojiang11@whut.edu.cn

Experimental details

Synthesis of CoNi@NC mesoporous nanowire arrays on carbon cloth. All the chemicals used are analytical grade without further purification. In a typical procedure, carbon cloths (CC) were cleaned and activated with dilute hydrochloric acid by ultrasonic wave for 30 min, then washed with acetone, deionized water and ethanol for several times to remove the residual acid. Next, 1 mmol $Co(NO_3)_2 \cdot 6H_2O$, 1 mmol $Ni(NO_3)_2 \cdot 6H_2O$, 6 mmol urea were dissolved in 40 mL deionized water under stirring for 5 min, then a piece of CC (2 cm*2 cm) was immersed into above solution. The CC and solution were transferred into 50 mL Teflon-lined autoclave and maintained at 120 °C for 6 h. After the autoclave was cooled down to room temperature, the coated CC was cleaned with ethanol for four times and dried at 70 °C in the air, resulting in CoO-NiO precursor nanowire arrays on CC. Then, the CoO-NiO mesoporous nanowire arrays on CC are obtained after calcined at 430 °C in argon for 3 h. The as-prepared CoO-NiO mesoporous nanowire arrays on CC and 2-Methylimidazole powders were treated at different temperatures (90, 120 and 150 °C) under low-pressure (~ 100 Pa) condition, obtaining CoO-NiO@ZIF nanowire arrays on carbon cloth. After treated at different temperatures (500, 600 and 700 °C) in H_2, the CoNi@NC-500, CoNi@NC-600 and CoNi@NC-700 samples were obtained.

Synthesis of CoSn@NC nanocubes. 1 mmol of $CoCl_2 \cdot 6H_2O$ and 1 mmol of sodium citrate were dissolved in 35 mL of deionized water, and then mixed with 5 mL of ethanol solution of $SnCl_4 \cdot 5H_2O$ (1 mmol) under stirring, followed by dropwise addition of 5 mL of aqueous solution of NaOH (2 M) at room temperature. After 1 h, 20 mL of aqueous solution of NaOH (8 M) was added to the above suspension and the reaction was lasted for 15 min at room temperature. And then the resulting pink $CoSn(OH)_6$ product was collected after washing with deionized water and alcohol for three times, respectively and dried at 70 °C in air. The as-prepared $CoSn(OH)_6$ nanocubes and 2-Methylimidazole powders were treated at 150 °C under low-temperature (~ 100 Pa) condition, obtaining $CoSn(OH)_6$@ZIF nanocubes. After treated at 550 °C in argon, the CoSn@NC nanocubes were obtained.

Synthesis of ZnO@NC nanorods. For a typical synthesis process, 0.55 g of $Zn(CH_3COO)_2 \cdot 2H_2O$ and 0.1 g of cetrimonium bromide (CTAB) powder were dissolved in 40 mL of ethylene glycol at room temperature under vigorous stirring for 1 h. 30 mL of 85% hydrazine hydrate was added, stirred for another 1 h and then the mixture was transformed into Teflon-line stainless steel vessel and heated 160 ^oC for 6 h. The precipitate was washed with alcohol for three times and dried at 70 °C in air for 6 h. Then, the as-prepared ZnO nanorods and 2-Methylimidazole powders were treated at 150 °C under low-temperature (~ 100 Pa) condition, obtaining ZnO@ZIF nanorods. Finally, after treated at 550 °C in argon, the ZnO@NC nanorods were obtained.

Synthesis of ZnO-$ZnMoO_3$@NC nanosheets. 1 mmol of $(NH_4)_6Mo_7O_{24} \cdot 4H_2O$ was dissolved in 100 mL of deionized water, followed by dropwise addition 8~12 mL of $NH_3 \cdot H_2O$ (2 M), under stirring at room temperature. 7 mmol of $Zn(NO_3)_2 \cdot 6H_2O$ was dissolved in 50 mL of deionnized water. And then the latter clear solution was added into the former solution dropwise and stirred for 2 h. The precipitate was collected by centrifugation, washed with water and alcohol for three times and dried at 70 °C for 6 h. In addition, when the precipitate was treated at 400 °C in air for 1 h, $Zn_3Mo_2O_9$ nanosheets were obtained. Then, the as-prepared $Zn_3Mo_2O_9$ nanosheets and 2-Methylimidazole powders were treated at 150 °C under low-temperature (~ 100 Pa) condition, obtaining $Zn_3Mo_2O_9$@MOF nanosheets. Finally, after treated at 500 °C in argon, the ZnO-$ZnMoO_3$@NC nanosheets were obtained.

Synthesis of CoO-MnO@NC nanotubes. In the typical synthesis, low-molecular-weight (98-99% hydrolyzed), middle-molecular-weight (86-89% hydrolyzed) and high-molecular-weight (98-99% hydrolyzed) PVA in a weight ratio of 3 : 2 : 1 (9.5 wt%) were dissolved in 20 mL deionized water. 3 mmol $Co(CH_3COO)_2 \cdot 4H_2O$ and 1.5 mmol $Mn(CH_3COO)_2 \cdot 4H_2O$ were added to the prepared PVA precursor. After the mixture was stirred at 80 °C for 5 h, a viscous, uniform, transparent solution was obtained. Subsequently, the precursor solution was electrospun at a constant flow rate and at a high voltage of 12 kV (electrospinning

equipment: SS-2534H from UCALERY Co., Beijing, China). The composite nanowires were collected on revolving aluminum foil. After drying at 80 °C for 12 h, the composite nanowires were heated up to 500 °C at 1 °C·min^{-1} and kept in air for 3 h, thereby obtaining $MnCo_2O_4$ mesoporous nanotubes. Then, the as-prepared $MnCo_2O_4$ mesoporous nanotubes and 2-Methylimidazole powders were treated at 150 °C for 3 h under low-temperature (~ 100 Pa) condition, obtaining $MnCo_2O_4$@ZIF mesoporous nanotubes. Finally, after treated at 500 °C in argon for 1 h and subsequent 280 °C in air for 2 h, the CoO-MnO@NC mesoporous nanotubes were obtained.

Synthesis of CoSn@C nanocubes. The $CoSn(OH)_6$ nanocubes were obtained by the same above process. Then, the $CoSn(OH)_6$ nanocubes and 1,4-dicarboxybenzene powders were treated at 220 °C for 5 h under low-temperature (~ 100 Pa) condition, obtaining $CoSn(OH)_6$@MOF. Finally, after treated at 550 °C in argon, the CoSn@C nanocubes were obtained.

Structural Characterizations. The crystallographic characteristics of the products were measured using a Bruker D8 Discover X-ray diffractometer equipped with a Cu Kα radiation source. SEM images were collected using a JEOL-7100F scanning electron microscope, and TEM images were collected using a JEM-2100F/Titan G2 60-300 transmission electron microscope. Energy-dispersive X-ray spectra were recorded using an Oxford IE250 system. Raman and FTIR spectra were obtained using Renishaw INVIA micro-Raman spectroscopy and Nicolet6700 measurements, respectively. The BET surface area was calculated from nitrogen adsorption isotherms collected at 77 K using a Tristar-3020 instrument. XPS measurement was conducted using an ESCALAB 250Xi instrument.

Computational details. All simulations on metal oxides were based on density functional theory (DFT) and carried out by using the projector augmented wave method (PAW) as implemented in the Vienna *ab initio* simulation package (VASP). The exchange and correlation functional was treated as generalized gradient approximation (GGA) of the Perdew-Burke-Ernzerhof (PBE) formula. The wave functions were expanded by using the plane waves up to a kinetic energy cutoff of

520 eV. Brillouin-zone integrations were approximated by using special *k*-point sampling of Monkhorst-Pack scheme with a *k*-point mesh resolution of $2\pi * 0.02$ $Å^{-1}$. The unit cell lattice vectors (unit cell shape and size) and atomic coordinates were fully relaxed until the force on each atom was less than 0.004 eV $Å^{-1}$.

Electrocatalysis measurements. All the electrochemical measurements were carried out in a three-electrode system on the electrochemical workstation (using CHI 760E). In the typical procedure, for the samples grown on CC, they were directly used as a binder-free working electrode for HER or OER testing, and the loadings of all samples grown on CC were measured about 2 mg cm^{-2}. For IrO_2/C and Pt/C catalyst ink, 8 mg of catalyst powders and 0.05 mL Nafion solutions were dispersed in 0.95 mL of water-isopropanol mixed solutions with the volume ratio of 5:14, and then treated by ultrasonic wave for 30 min to form homogeneous ink. 0.25 mL of above homogeneous ink was uniformly smeared onto a piece of CC within the area of 1 cm^{-2}, the dried CC with IrO_2/C or Pt/C-based catalysts coating were obtained as working electrodes. The saturated calomel and graphite rod were used as reference electrode (after calibration) and counter electrode, respectively. Linear sweep voltammetry (LSV) with a scan rate of 5 mV s^{-1} was conducted in 1 M KOH solution for both HER and OER. The long-term stabilities for all samples were carried out by using Chronopotentiometry in a fixed current density of 10 mA cm^{-2} (absolute value). Electrochemical impedance spectroscopy (EIS) measurements were tested using A. C. Impedance at a fixed overpotential (100 mV vs. RHE for HER and 300 mV vs. RHE for OER) in a frequency range of 0.1 to 1000 Hz with an applied AC voltage of 5 mV. Potentials were referenced to a reversible hydrogen electrode (RHE) by adding a value of (0.059*pH+0.2415) V. All LSV curves were performed in iR compensated form and all potentials were against RHE.

Lithium storage measurements. The anode electrodes were composed of 80 wt% CoO-MnO@NC or $MnCo_2O_4$, 10 wt% acetylene black, and 10 wt% carboxymethyl cellulose (CMC) binder. After coating onto copper foil, the electrode film was uniformly cut into ~ 0.5 cm^2 (area) round slices, weighing a total of ~ 1.2 mg; the

corresponding areal mass loading was 2.4 mg·cm^{-2}. 2,016 coin cells were assembled in a glovebox filled with pure argon gas. Lithium foil was used as the counter electrode and the separator was Celgard 2400 microporous membrane. 1 M lithium hexafluorophosphate ($LiPF_6$) solution in ethylene carbon (EC)-dimethyl carbonate (DMC) (1:1 v/v) was used as the electrolyte. Galvanostatic charge-discharge measurements were performed using a multichannel battery testing system (LAND CT2001A). CVs and electrochemical impedance spectra were collected at room temperature using an Autolab potentiostat/galvanostat.

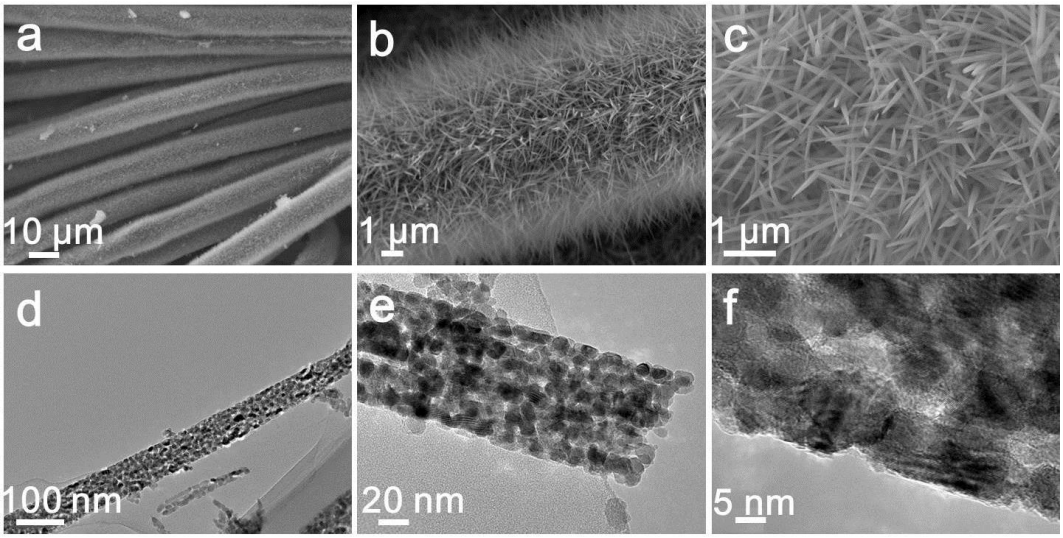

Figure S1. SEM (a-c) and TEM (d-f) images of CoO-NiO mesoporous nanowire arrays on carbon cloth.

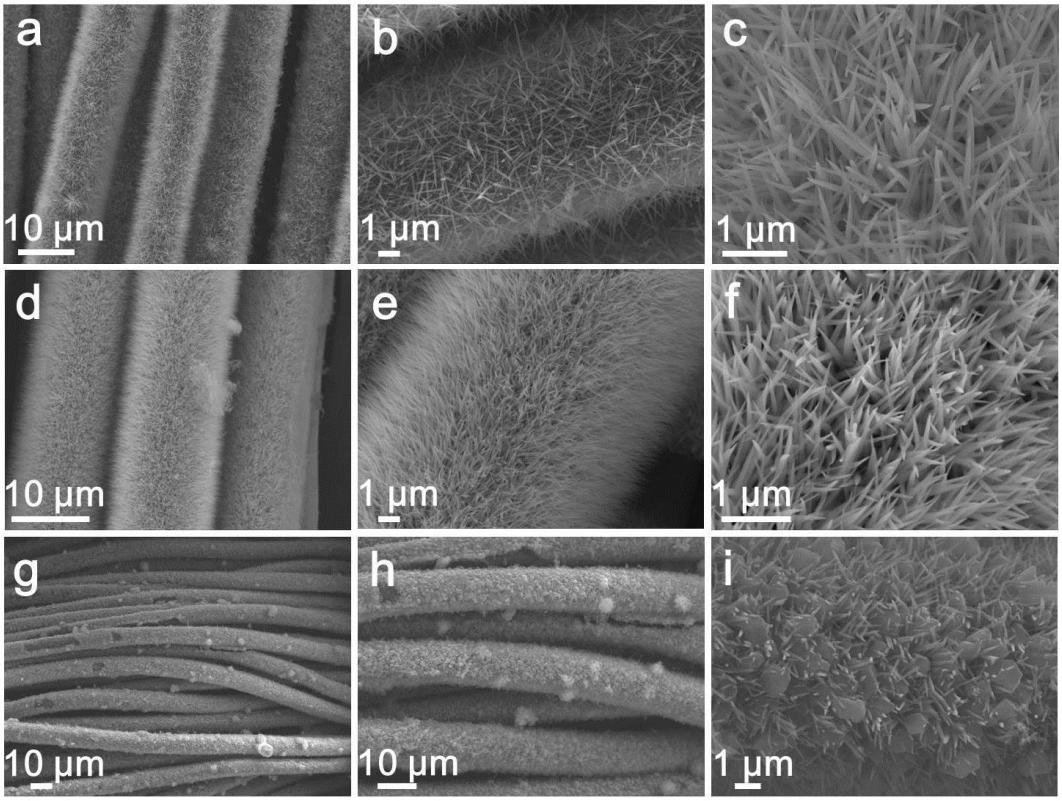

Figure S2. Morphology characterizations of ZIF-confined CoO-NiO mesoporous nanowire arrays on carbon cloth after treated at different temperatures by low-temperature vapor superassembly. (a-c) SEM images after treated at 80 °C for 8h. (d-f) SEM images after treated at 120 °C for 8h. (g-i) SEM images after treated at 150 °C for 8h.

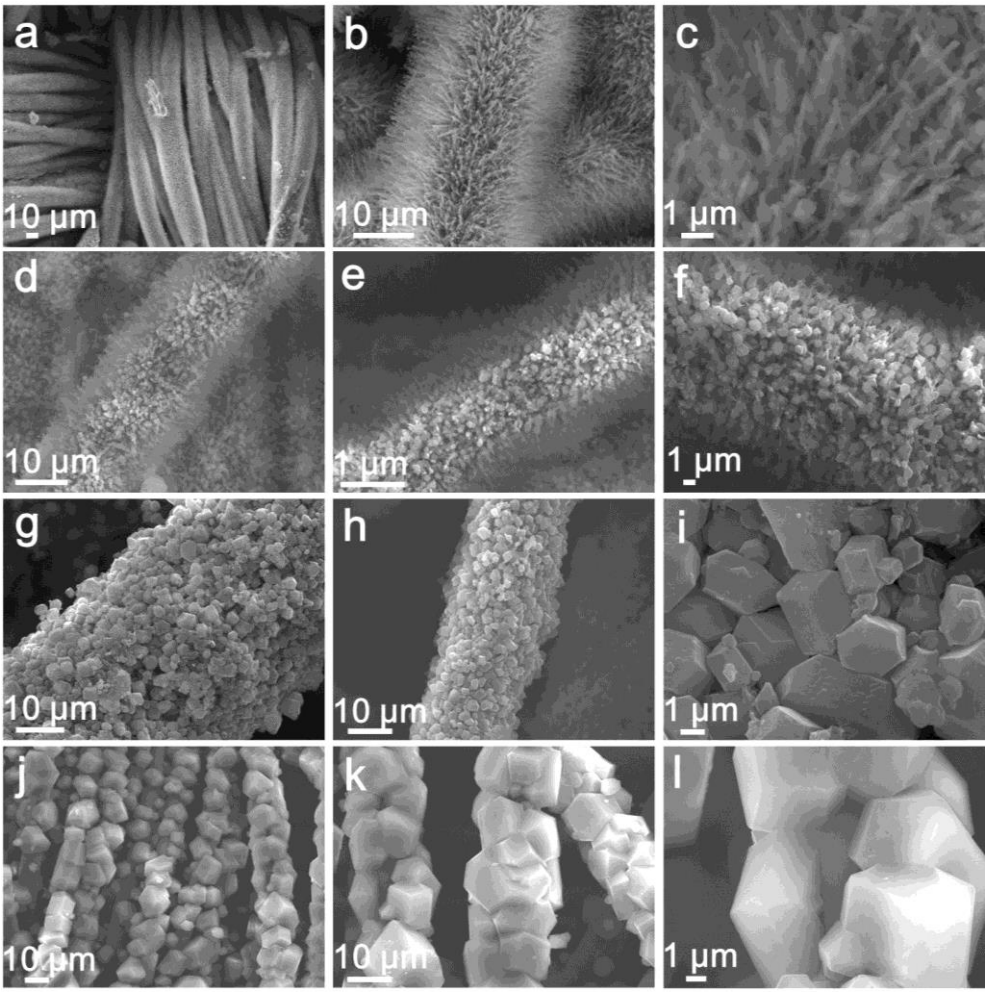

Figure S3. Morphology evolution of ZIF-confined CoO-NiO precursor nanowire arrays on carbon cloth after treated at different reaction times by low-temperature vapor superassembly. (a-c) SEM images after treated at 150 °C for 15 min. (d-f) SEM images after treated at 150 °C for 30 min. (g-i) SEM images after treated at 150 °C for 1 h. (j-l) SEM images after treated at 150 °C for 2 h.

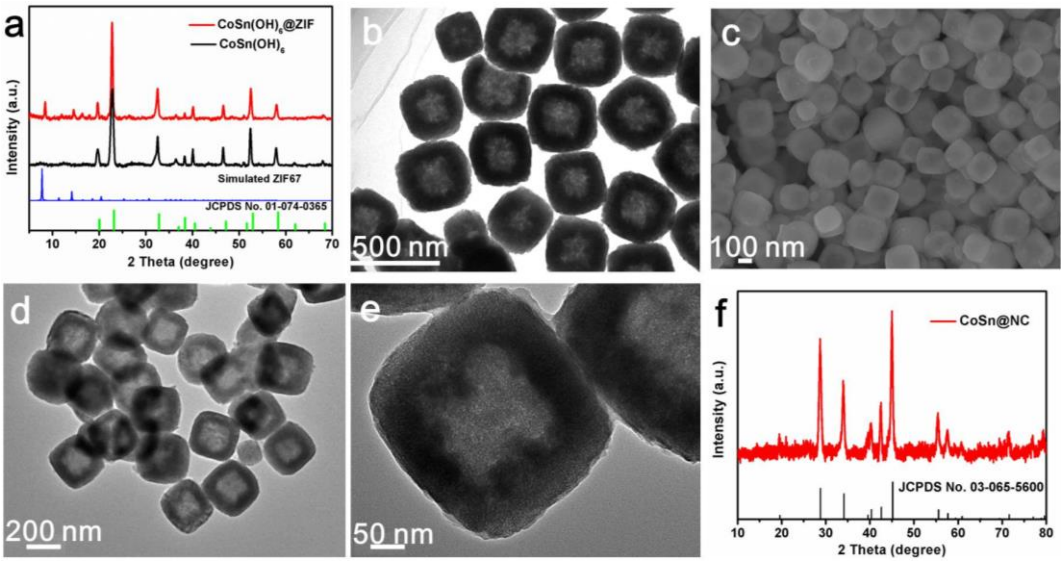

Figure S4. (a) XRD pattern of $CoSn(OH)_6$ and $CoSn(OH)_6$@ZIF nanocubes. (b) TEM image of $CoSn(OH)_6$ nanocubes. (c-e) SEM and TEM images of $CoSn(OH)_6$@ZIF nanocubes. (f) XRD pattern of CoSn@NC nanocubes.

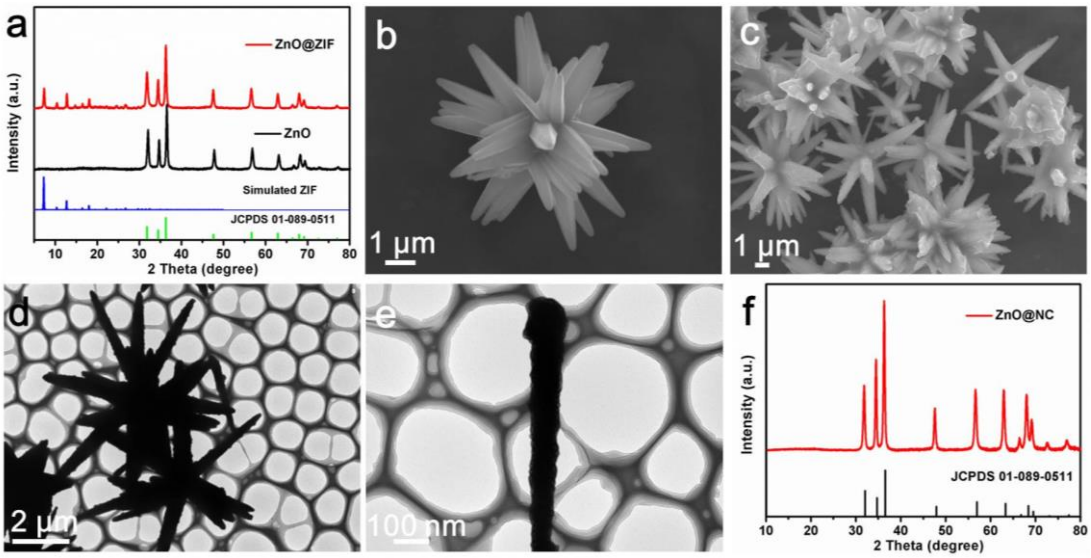

Figure S5. (a) XRD pattern of ZnO and ZnO@ZIF nanorods. (b) SEM image of ZnO nanorods. (c-e) SEM and TEM images of ZnO@ZIF nanorods. (f) XRD pattern of ZnO@NC nanorods.

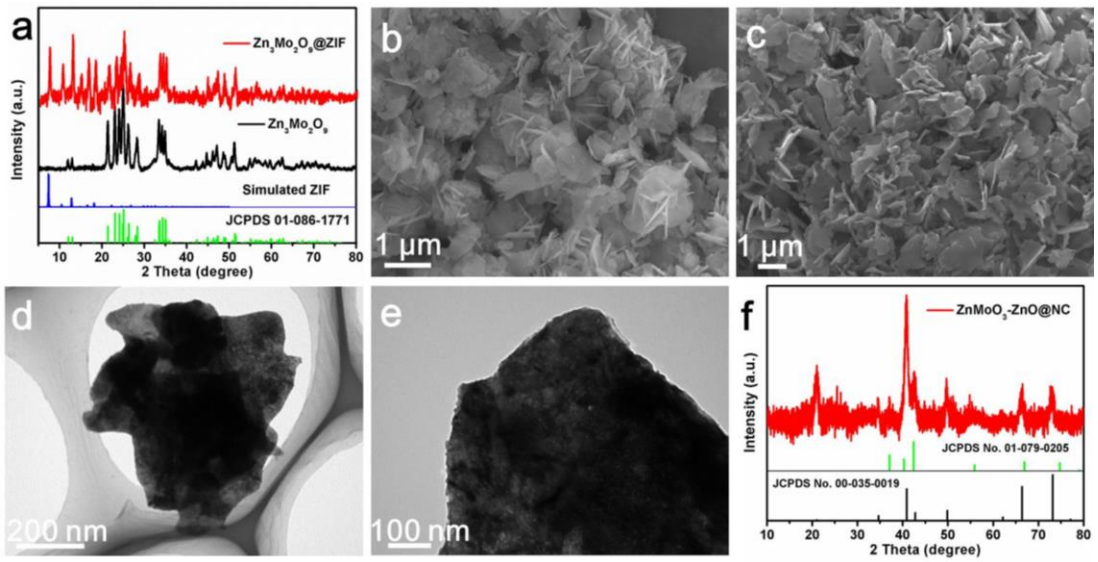

Figure S6. (a) XRD pattern of $Zn_3Mo_2O_9$ and $Zn_3Mo_2O_9$@ZIF nanosheets. (b) SEM image of $Zn_3Mo_2O_9$ nanosheets. (c-e) SEM and TEM images of $Zn_3Mo_2O_9$@ZIF nanosheets. (f) XRD pattern of $ZnMoO_3$-ZnO@NC nanosheets.

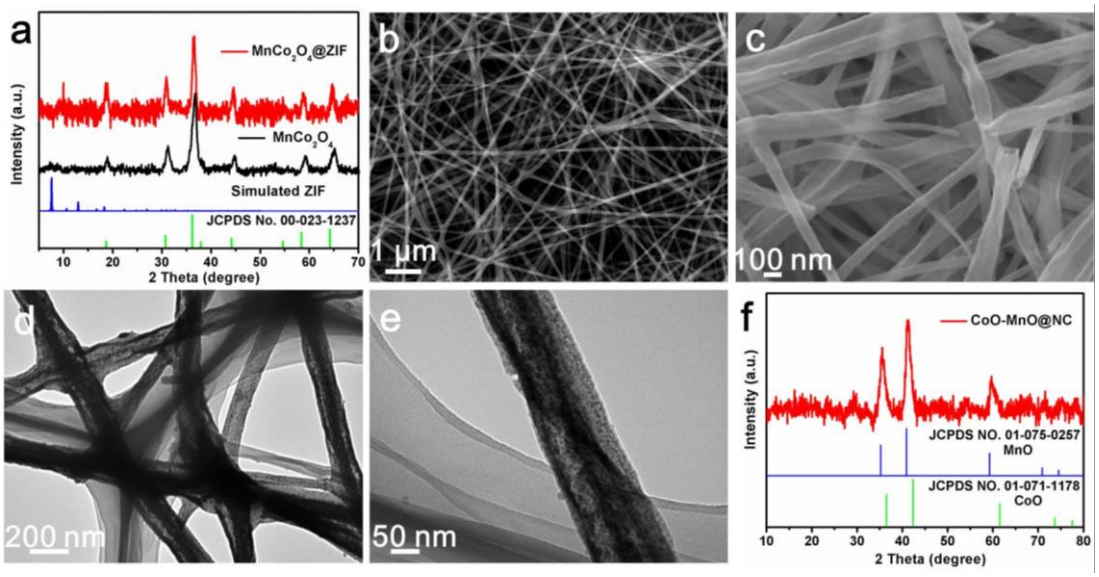

Figure S7. (a) XRD pattern of $MnCo_2O_4$ and $MnCo_2O_4$@ZIF nanotubes. (b) SEM image of $MnCo_2O_4$ nanotubes. (c-e) SEM and TEM images of $MnCo_2O_4$@ZIF nanotubes. (f) XRD pattern of CoO-MnO@NC nanotubes.

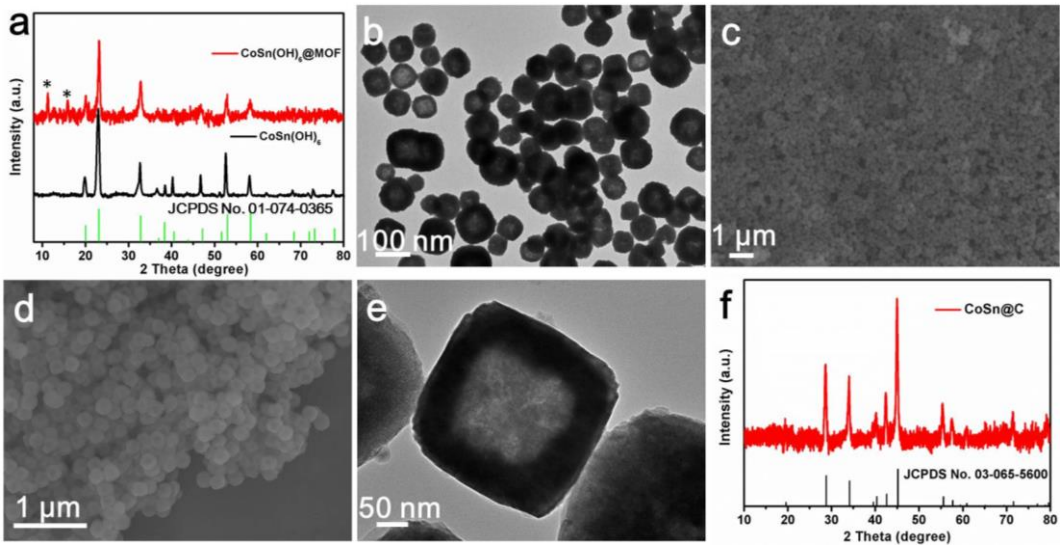

Figure S8. (a) XRD pattern of $CoSn(OH)_6$ and $CoSn(OH)_6$@MOF nanocubes. (b) TEM image of $CoSn(OH)_6$ nanocubes. (c-e) SEM and TEM images of $CoSn(OH)_6$@MOF nanocubes. (f) XRD pattern of CoSn@C nanocubes.

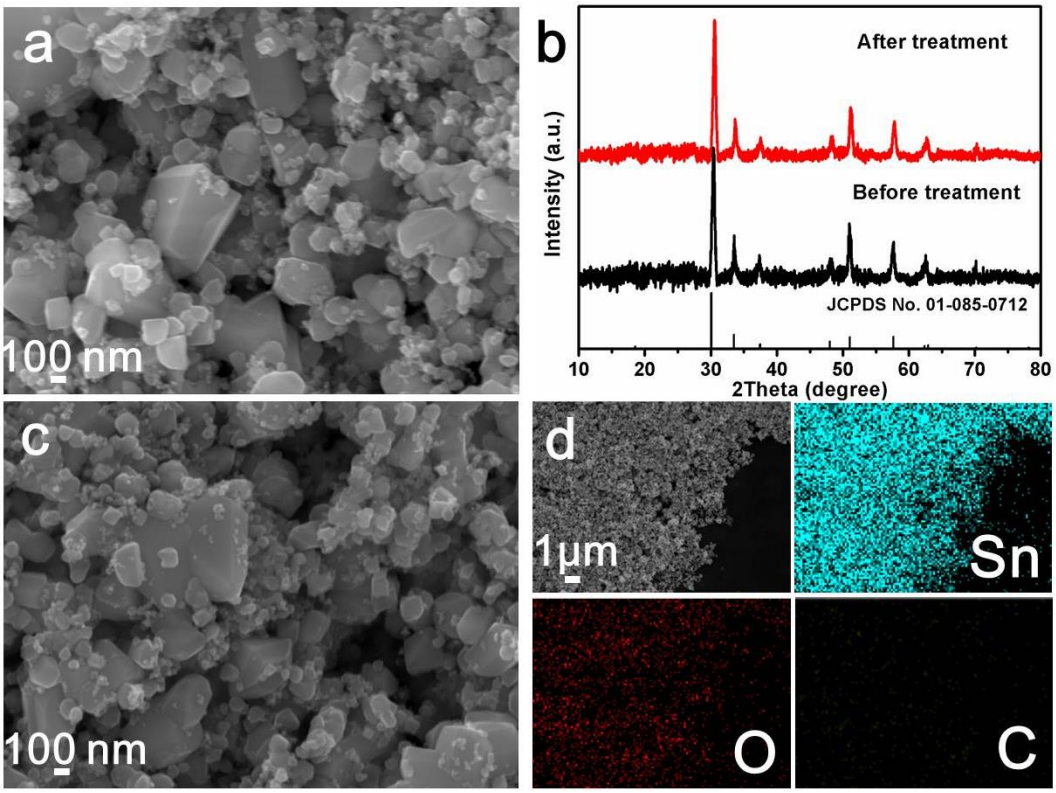

Figure S9. (a) SEM image of SnO nanoparticles. (b) XRD patterns of SnO nanoparticles before and after low-pressure vapor superassembly treatment. (c) SEM image of SnO nanoparticles after treatment. (d) SEM image and elemental mapping

images of SnO nanoparticles after treatment.

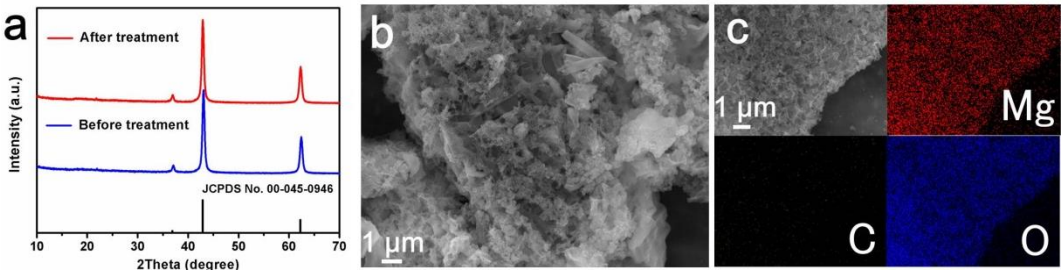

Figure S10. (a) XRD patterns of MgO nanoparticles before and after low-temperature vapor superassembly treatment. (b) SEM image of MgO nanoparticles after treatment. (c) SEM image and elemental mapping images of MgO nanoparticles after treatment.

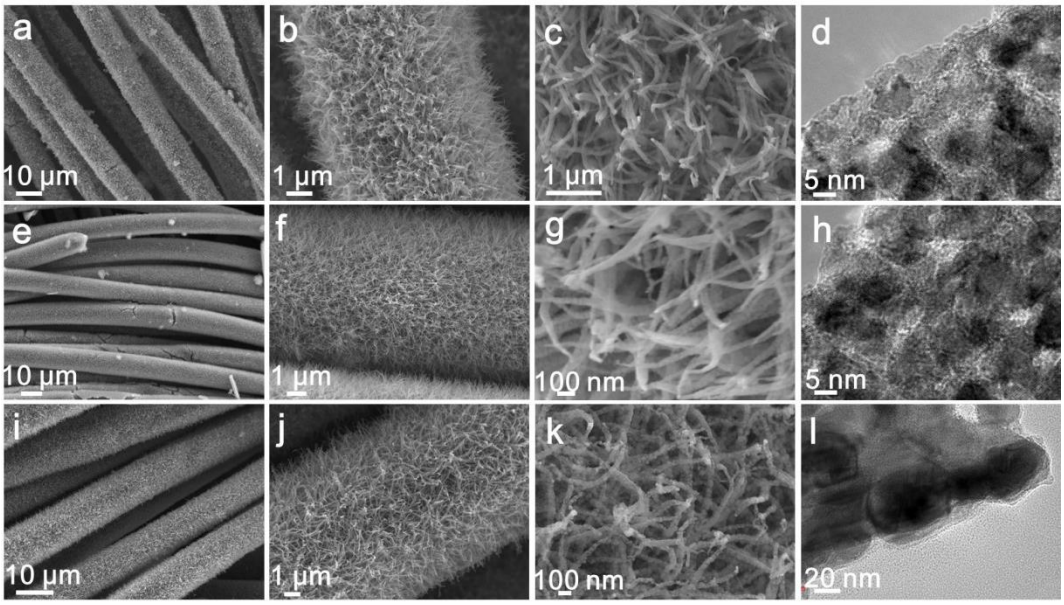

Figure S11. Morphology characterizations of various CoNi@NC mesoporous nanowire arrays on carbon cloth. (a-d) SEM and TEM images of CoNi@NC-500 sample. (e-h) SEM and TEM images of CoNi@NC-600 sample. (i-l) SEM and TEM images of CoNi@NC-700 sample.

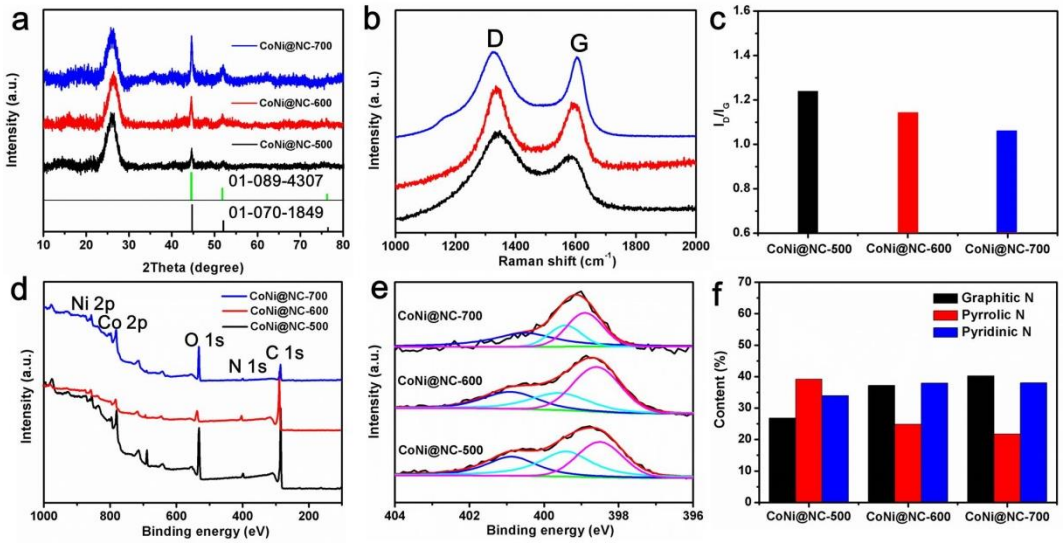

Figure S12. Structural characterizations of various CoNi@NC mesoporous nanowire arrays on carbon cloth. (a) XRD patterns. (b, c) Raman spectra and the corresponding I_D/I_G ratios. (d) XPS spectra. (e, f) High-resolution N 1s XPS spectra and the corresponding contents of pyridinic N, pyrrolic N and graphitic N.

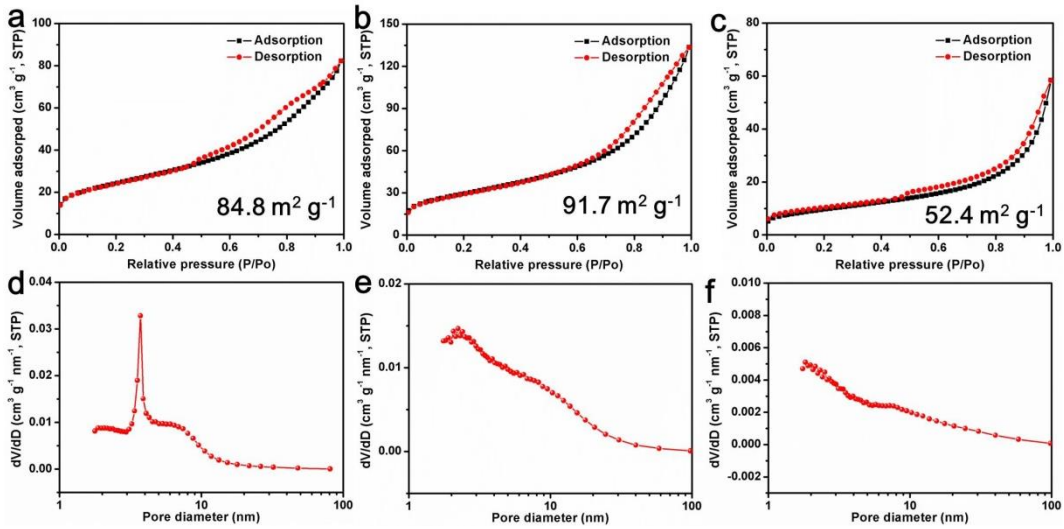

Figure S13. BET and BJH curves of various CoNi@NC mesoporous nanowire arrays on carbon cloth. (a, d) BET and BJH curves of CoNi@NC-500 sample. (b, e) BET and BJH curves of CoNi@NC-600 sample. (c, f) BET and BJH curves of CoNi@NC-700 sample.

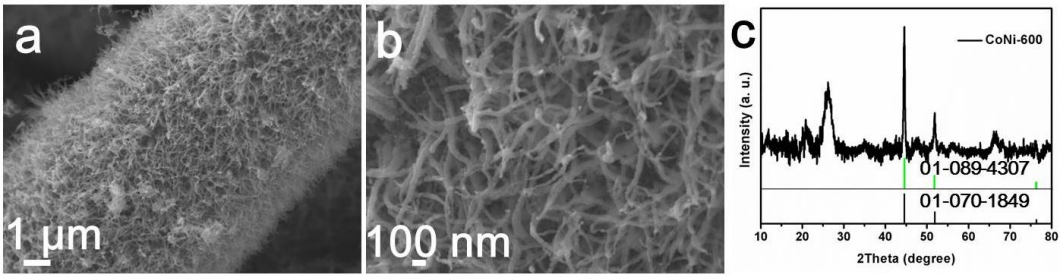

Figure S14. Characterizations of CoNi-600 sample. (a, b) SEM images. (c) XRD pattern.

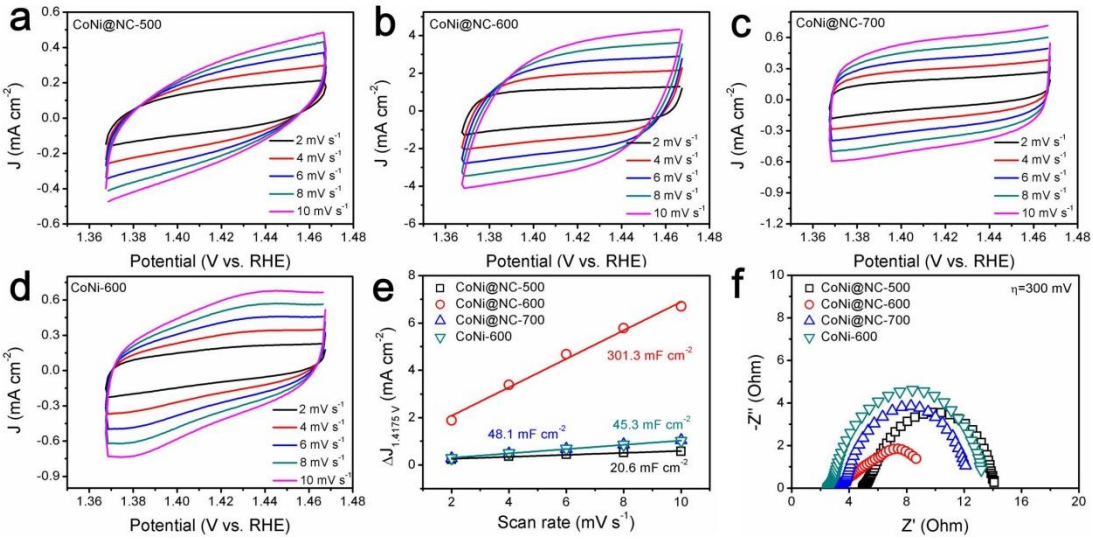

Figure 15. (a-d) Cyclic voltammograms (CVs) of CoNi@NC-500, CoNi@NC-600, CoNi@NC-700 and CoNi-600 samples at different scan rates from 2 to 10 mV s^{-1}, respectively. (e) CV current density versus scan rate for CoNi@NC-500, CoNi@NC-600, CoNi@NC-700 and CoNi-600 samples. (f) The Nyquist plots of CoNi@NC-500, CoNi@NC-600, CoNi@NC-700 and CoNi-600 samples at the overpotential of 300 mV during OER testing.

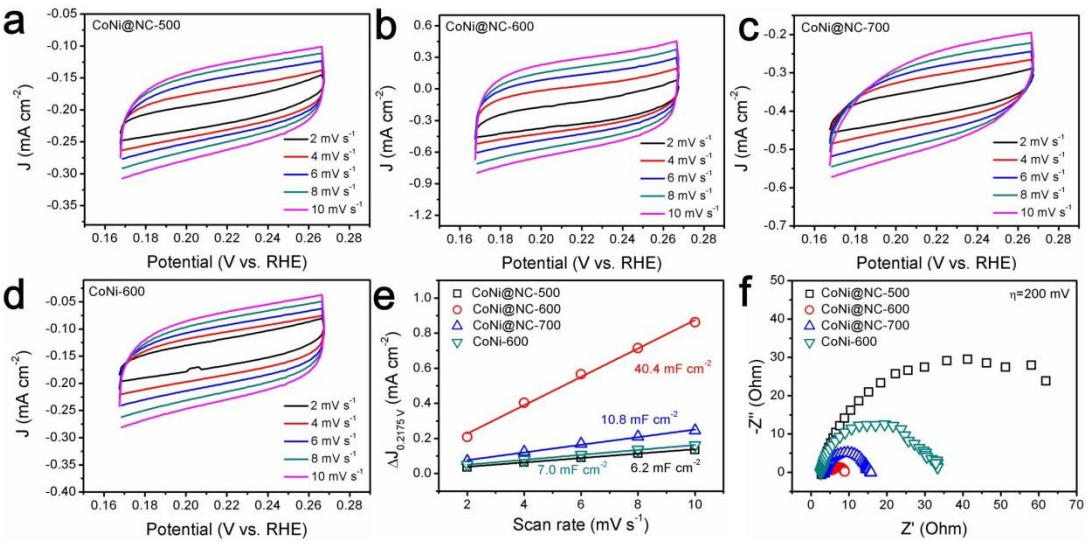

Figure S16. (a-d) Cyclic voltammograms (CVs) of CoNi@NC-500, CoNi@NC-600, CoNi@NC-700 and CoNi-600 samples at different scan rates from 2 to 10 mV s^{-1}, respectively. (e) CV current density versus scan rate for CoNi@NC-500, CoNi@NC-600, CoNi@NC-700 and CoNi-600 samples. (f) The Nyquist plots of CoNi@NC-500, CoNi@NC-600, CoNi@NC-700 and CoNi-600 samples at the overpotential of 200 mV during HER testing.

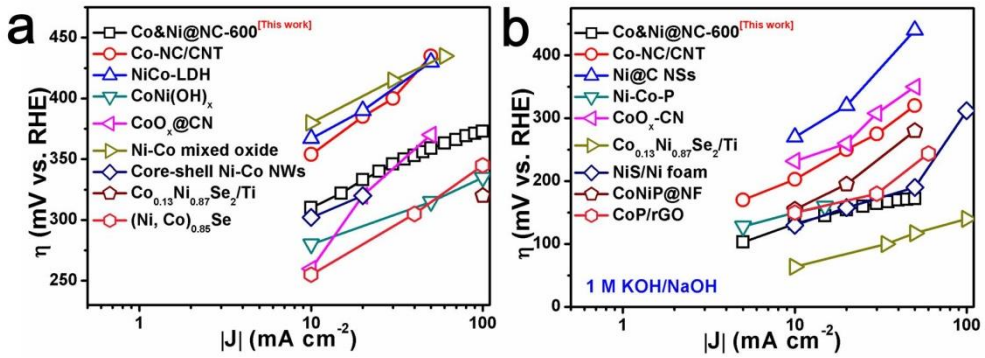

Figure S17. (a) The comparisons of various current electrocatalysts for OER. (b) The comparisons of various current electrocatalysts for HER.

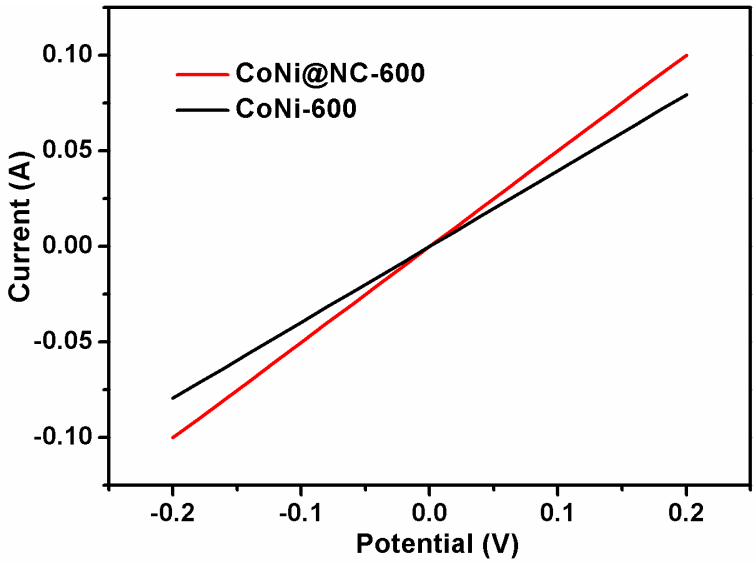

Figure S18. I-V curves of CoNi@NC-600 and CoNi-600 powders via a standard four-probe method on pressed pellets

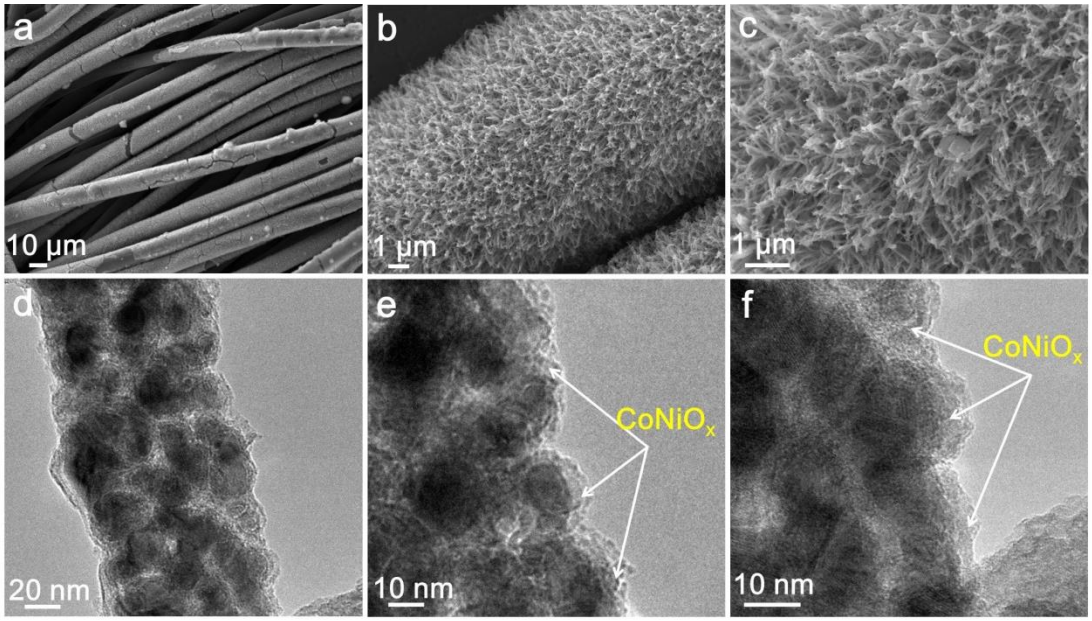

Figure S19. SEM images (a-c) and TEM images (d-f) of CoNi@NC-600 sample after OER test.

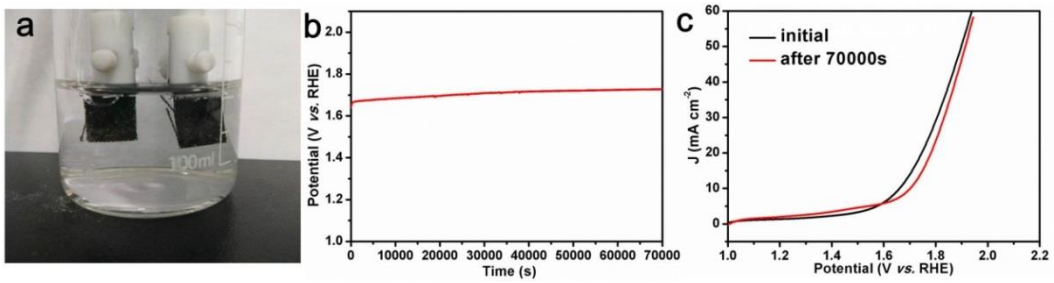

Figure S20. Electrocatalystic performances of CoNi@NC-600 sample for full water splitting. (a) The optical image of the reaction equipment. (b) Chronopotentiometry response under a series constant 10 mA cm^{-2} current density. (c) LSV curves before and after a stability test.

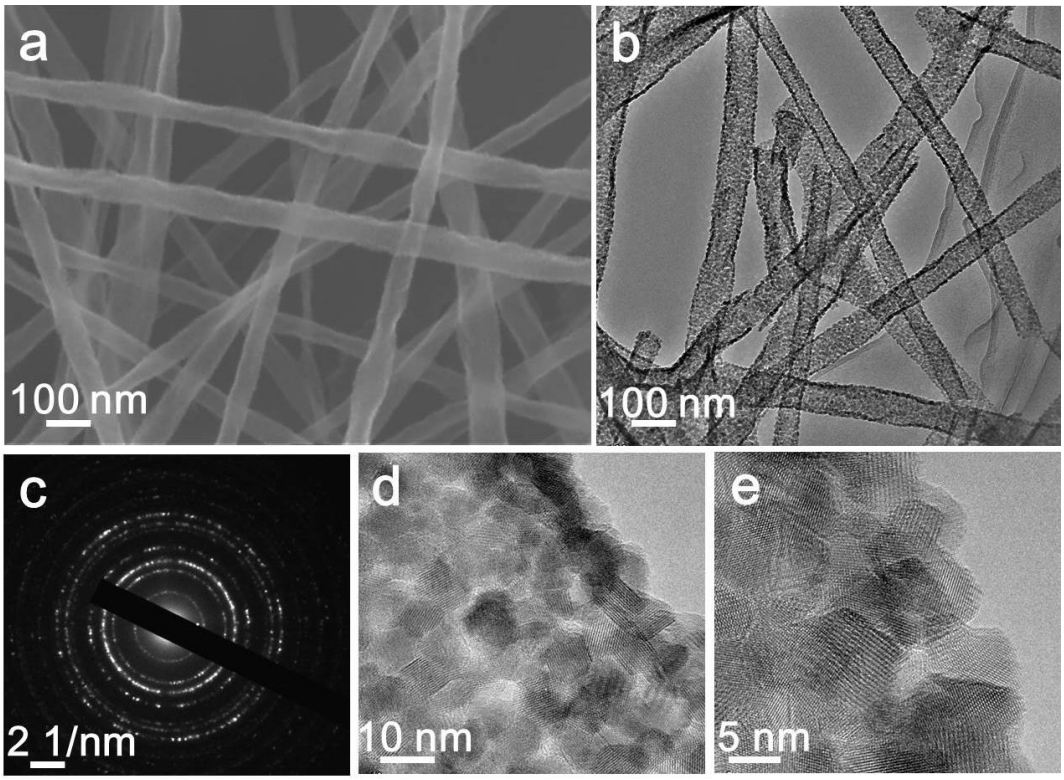

Figure S21. Morphology characterizations of $MnCo_2O_4$ mesoporous nanotubes. (a) SEM image. (b) TEM image. (c) SAED pattern. (d, e) HRTEM images.

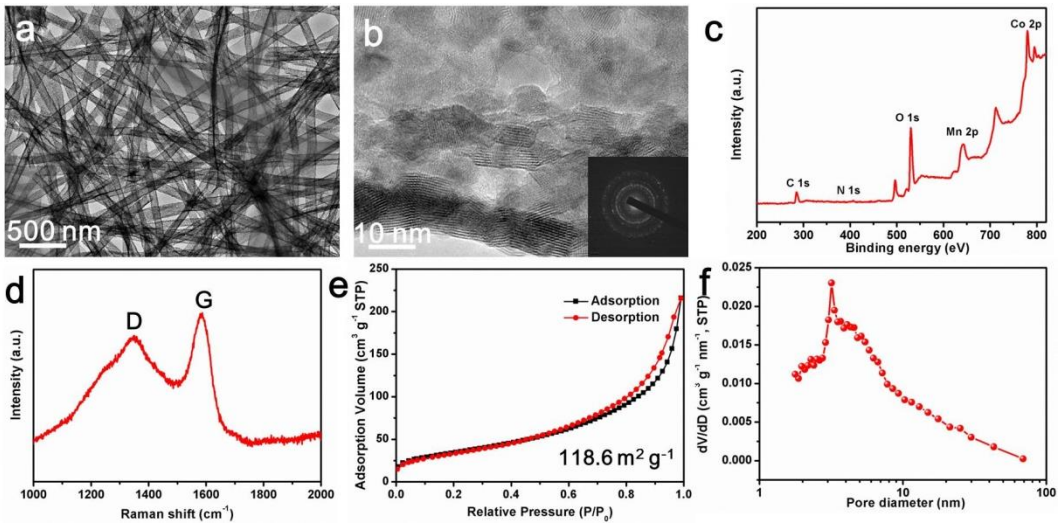

Figure S22. Characterizations of CoO-MnO@NC mesoporous nanotubes. (a) TEM image. (b) HRTEM image; Inset of (b) is SAED pattern. (c) XPS spectrum. (d) Raman spectrum. (e, f) BET and BJH curves.

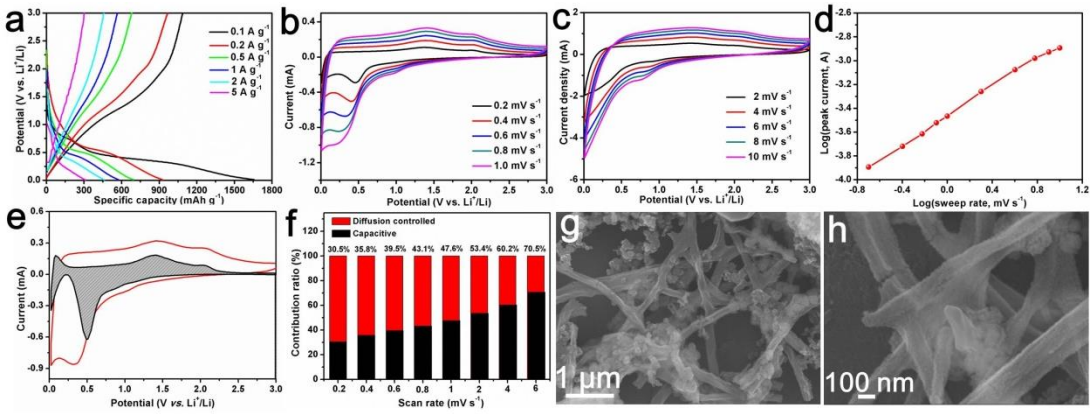

Figure S23. Electrochemical performances of CoO-MnO@NC mesoporous nanotubes in LIBs. (a) Charge and discharge curves at various current densities. (b, c) CV curves at various scan rates ranging from 0.2 to 10 mV s^{-1}. (d) Determination of the b-value using the relationship between peak current and scan rate. (e) Separation of the capacitive and diffusion currents at a scan rate of 1.0 mV s^{-1}. (f) Contribution ratio of the capacitive and diffusion-controlled charge versus scan rate. (g, h) SEM images after 100 cycles at 0.2 A g^{-1}.

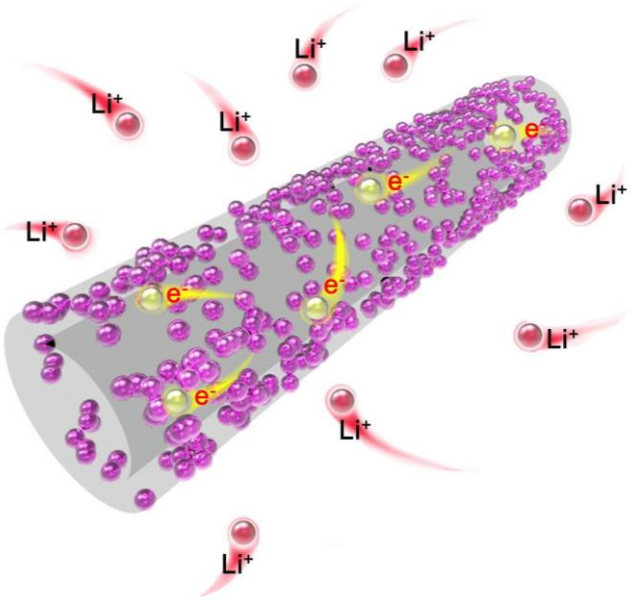

Figure S24. Schematic illustration of CoO-NiO@NC mesoporous nanotubes with efficient ion and electron transport for LIBs.

Table S1. A summary of the bonding energies of various metal oxides on the basis of DFT calculations.

Metal oxides	Bonding energy (eV)	Bonding energy (KJ mol^{-1})
CoO	**2.72**	**261.8**
ZnO	**2.90**	**279.8**
MgO	**5.49**	**529.1**
CaO	**5.95**	**573.2**
BaO	**4.97**	**479.1**
SrO	**5.49**	**529.0**
NiO	**3.39**	**326.3**
SnO	**2.59**	**249.6**
SiO_2	**8.45**	**814.9**

Table S2. A comparison of our work and current main synthetic methods for

nanostructured coatings.

Coating methods	Coating sources	Advantages	Disadvantages	References
Vapor superassembly	**MOFs**	**● Precise control ● High quality coatings ● Without limited substrates ● High yield ● Low cost ● Simple manipulation**	**---**	**Our work**
Solution-based synthesis	**MOFs**	**● Simple manipulation● Low cost ● Relative high yield**	**● Solvent consuming ● Hard control on uniform coatings**	*Chem*, 2017, **2**, 791-802.
Chemical vapor deposition	**Toluene**	**● Precise control ● High quality coatings ● Without limited substrates**	**● High cost ● Low yield ● Complex manipulation ● Hard to obtain complex compositions**	*Energy Environ. Sci.*, 2015, **8**, 1889-1904.
Atomic layer deposition	**Metal organic compounds**	**● Precise control ● High quality coatings ● Without limited substrates**	**● High cost ● Low yield ● Complex manipulation ● Hard to obtain complex compositions**	*Energy Environ. Sci.*, 2015, **8**, 1889-1904.
In situ polymerization	**Aniline**	**● Uniform coating ● Tunable thickness ● Without limited substrates**	**● High cost ● Low yield ● High toxicity**	*J. Am. Chem. Soc.*, 2013, **135**, 16736-16743.
Hydrothermal synthesis	**Glucose**	**● Simple manipulation ● Easy control**	**● High temperature ● Solvent**	*J. Am. Chem. Soc.*, 2003, **125**, 5652-5653.

	● Low cost	**consuming** **● Relative low yield** **● Hard control on uniform coatings**	

Table S3. The comparisons of our work and previous reports in different nanostructured mixed metal oxides for LIBs.

Morphology	**Voltage range (V)**	**Current density (mA g^{-1})**	**Cycle number**	**Residual capacity (mAh g^{-1})**	**Capacity retention**	**Reference**
CoO-MnO@NC mesoporous nanotubes	**0.01-3**	**100** **2000**	**200** **1000**	**1153** **650**	**91.1%** **> 100%**	**Our work**
Hollow $CoMn_2O_4$ microspheres	0.01-3	1000	50	585	73%	S1
Hollow $CoMn_2O_4$ nanocloth	0.01-3	400	100	506	63%	S2
$MnCo_2O_4$ microspheres	0.01-3	400	200	553	58%	S3
Core-shell ellipsoidal $MnCo_2O_4$	0.01-3	100	70	750	88%	S4
Hollow $CoMn_2O_4$ microspheres	0.01-3	200	25	706	77%	S5
$CoMn_2O_4$ nanorods	0.01-3	200	100	510	57%	S6
Yolk-shell $CoMn_2O_4$	0.01-3	800	40	579	80%	S7

microspheres						
$CoMn_2O_4$ nanotubes	0.01-3	100	50	800	88%	S8
Double-shelled $CoMn_2O_4$ microcubes	0.01-3	200	50	624	76%	S9
$CoMn_2O_4$ tube-in-tube nanotubes	0.01-3	2000	500	503	89%	S10

References

[S1] L. X. Zhang, Y. L. Wang, H. F. Jiu, W. H. Zheng, J. X. Chang, G. F. He, *Electrochimica Acta*, 2015, **182**, 550-558.

[S2] G. R. Yang, X. Xu, W. Yan, H. H. Yang, S. J. Ding, *Electrochimica Acta*, 2014, **137**, 462-469.

[S3] C. C. Fu, G. S. Li, D. Luo, X. S. Huang, J. Zheng, L. P. Li, *ACS Appl. Mater. Interfaces*, 2014, **6**, 2439-2449.

[S4] G. Y. Huang, S. M. Xu, Z. H. Xu, H. Y. Sun, L. Y. Li, *ACS Appl. Mater. Interfaces*, 2014, **6**, 21325-21334.

[S5] J. F. Li, S. L. Xiong, X. W. Li, Y. T. Qian, *Nanoscale*, 2013, **5**, 2045-2054.

[S6] L. J. Wang, B. Liu, S. H. Ran, L. M. Wang, L. N. Gao, F. Y. Qu, D. Chen, G. Z. Shen, *J. Mater. Chem. A*, 2013, **1**, 2139-2143.

[S7] M. H. Kim, Y. J. Hong, Y. C. Kang, *RSC Adv.*, 2013, **3**, 13110-13114.

[S8] S. M. Hwang, S. Y. Kim, J.-G. Kim, K. J. Kim, J.-W. Lee, M.-S. Park, Y.-J. Kim, M. Shahabuddin, Y. Yamauchi, J. H. Kim, *Nanoscale*, 2015, **7**, 8351-8355.

[S9] L. Zhou, D. Y. Zhao, X. W. Lou, *Adv. Mater.*, 2012, **24**, 745-748.

[10] J. S. Meng, C. J. Niu, X. Liu, Z. A. Liu, H. L. Chen, X. P. Wang, J. T. Li, W. Chen, X. F. Guo, L. Q. Mai, *Nano Res.*, 2016, **9**, 2445-2457.